Journal of Intelligent & Robotic Systems (2021) 102: 43
https://doi.org/10.1007/s10846-021-01408-z

REGULAR PAPER

Bio-Inspired Feedback Linearized Adaptive Control For a Thrust Vectoring Free-Flyer Vehicle

Andres Perez[1] · **Hever Moncayo**[1]

Received: 18 November 2020 / Accepted: 27 April 2021 / Published online: 24 May 2021

Abstract
Intelligent unmanned robotic systems have recently gained popularity due to their ability to potentially explore inaccessible and dynamically changing environments. In these environments, these vehicles might be subjected to unique types of disturbances that may lead to mission performance degradation. This paper describes the design, development and proof of concept of a novel adaptive control that combines concepts from model reference and feedback linearization and it is augmented via nonlinear bounded functions typical in immune system responses of living organisms. Proof of stability of the proposed control law using Circle Criterion is presented. Numerical hardware in the loop simulations along with actual implementation are performed using a gimbaled mini-free flyer vehicle that uses thrust vectoring control actuation. A set of performance index metrics are used to quantify and assess the performance of the adaptive control system which shows stabilizing capabilities in the presence of system disturbances and uncertainties.

Keywords Adaptive control · Artificial intelligence · Aerospace vehicles

1 Introduction

The increase in the operational capabilities of robotic systems for space exploration missions demands a significant improvement in their level of reliability, effectiveness, and efficiency. Advanced autonomous space systems require advanced intelligent systems with the ability to perform complex information processing, reconfiguration and decision making to optimize performance within complex, unstructured and dynamic, sometimes unknown, operating environments. These technologies are expected to increase autonomy by maintaining control of the mobile robots while rejecting undesired conditions caused by unexpected uncertainties and disturbances. Therefore, exploration of celestial bodies imposes potential challenges that require the development of new technologies.

✉ Hever Moncayo
hever.moncayo@erau.edu

Andres Perez
ae.perezrocha@gmail.com

[1] Embry-Riddle Aeronautical University, 1 Aerospace Blvd, Daytona Beach, FL, 32128 USA

Current efforts by the authors have been focused on developing technologies to enhance space exploration missions through the design of novel flying robotic vehicles [1–4]. These vehicles, known as Extreme Access Flyers (EAF), are powered by cold-gas jets with mobility and autonomy capabilities. They feature Thrust Vectoring Control (TVC) actuation to increase maneuverability with limited power consumption [5]. Early versions of these EAF prototypes were equipped with propellers and brushless motors, while a newer version, named Gimbaled Mini-Free Flyer (GMFF), features ducted fans with thrust vectoring capabilities (Fig. 1 left). These prototypes were developed to support validation and verification of intelligent control algorithms for the next generation of space exploration robotic systems. One example is the extreme-access spacecraft flyer system that is powered with cold gas and uses thrust vectoring actuation as shown in Fig. 1-right [6].

During space exploration tasks EAFs might be exposed to uncertainties and disturbances that could compromise the success of the mission. Therefore, disturbance rejection is still a challenge that must be addressed to increase autonomy and operation performance. Of particular attention is the development of technologies that can provide timely compensation to system upset conditions to maintain system stability [7–10]. Several adaptive control techniques have widely investigated to resolve the problem of

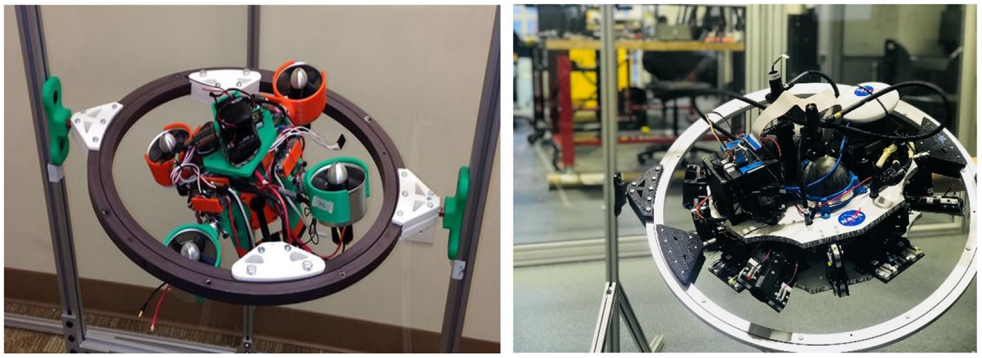

Fig. 1 GMFF Testbed (Left), EASY spacecraft prototype (Right)

disturbance rejection in aerospace systems. Although still a matter of extensive research, adaptive control theory has demonstrated to have the potential to increase autonomy, resiliency and versatility of the system while providing a robust solution when the system diverges outside bounds of nominal design.

Fault tolerant adaptive control techniques inspired by bio-mechanisms has recently been an active area of research. These techniques have shown to address the multidimensionality problem typical of nonlinear aerospace systems when detecting and accommodating to sub-system malfunctions or upset conditions [11–14]. Addressing adverse dynamics and mitigating their effects using intelligent control laws could represent a key aspect in the development of next generation of aerospace vehicles and its safety operation.

Algorithms inspired by biological mechanisms represent alternative solutions in the design of adaptive systems. In particular, Artificial Immune System (AIS) has been known to have special characteristics, that combined with other machine learning techniques, can provide a framework and the basis for the development of intelligent algorithms with self-adaptiveness, strong robustness and cognitive capabilities [15, 16]. Such characteristics have provided the basis for the emergence of this new computational paradigm in artificial intelligence. Different mechanisms of immune system components are the source of inspiration for techniques in a wide set of engineering applications including data mining [17], distributed and cooperative control [18–21], parameter optimization [22, 23], fault diagnosis and health management [24, 25], control scheduling [26, 27], path planning [28, 29], computer network protection [30], and adaptive control [31]. In recent years, although new models and applications are currently being developed and existing methods are improved continuously, the field is still relatively young, not well defined and no systematic theoretical background yet supports the AIS.

The main contribution of the work presented in this paper is the design, implementation and theoretical stability analysis of a bio-inspired adaptive control architecture for GMFF attitude control. The proposed control is primarily based on a hybrid approach that uses feedback linearization as a first layer and it is augmented by a novel Model-Reference Adaptive Immune System (MRAIS) at a higher level for disturbance rejection. The first layer guarantees that the closed loop response behaves as close as possible to a desired system dynamics while the higher adaptive layer features a set of nonlinear functions that describe the response of the immune system of living organisms to external attacks. Successful implementation of the proposed control laws, both in hardware in the loop and on a real prototype, demonstrates the effectiveness of the adaptive architecture to compensating bounded disturbances such as thruster failures and variation of vehicle's inertias.

The paper is organized as follows. Section 2 includes an introduction to the GMFF vehicle dynamic model followed by Section 3 that describes the baseline control law design. Section 4 includes derivation of the proposed adaptive control augmentation and provides a theoretical analysis of the stability of the system. Section 5 discusses numerical simulation results and describe the performance metrics used to assess the capabilities of the control laws. Description of the experimental setup and implementation results are presented in Section 6. Finally, some conclusions are specified in Section 7, followed by acknowledgments and a list of references.

2 Vehicle and Thrust Vectoring Dynamics

A free body diagram of the GMFF is shown in Fig. 2. The GMFF features four ducted fans [32, 33] where each thruster has the capability to actuate with a tilting angle defined by γ. Assuming rigid body and neglecting the aerodynamics forces, Eqs. 1 and 2 represent the forces and moments acting on the vehicle in body-fixed reference frame.

$$m\dot{\mathbf{V}}_b + \boldsymbol{\omega} \times m\mathbf{V}_b = \mathbf{F_T} + \mathbf{F}_g \tag{1}$$

$$J\dot{\boldsymbol{\omega}} + \boldsymbol{\omega} \times J\boldsymbol{\omega} = \mathbf{M}_T \tag{2}$$

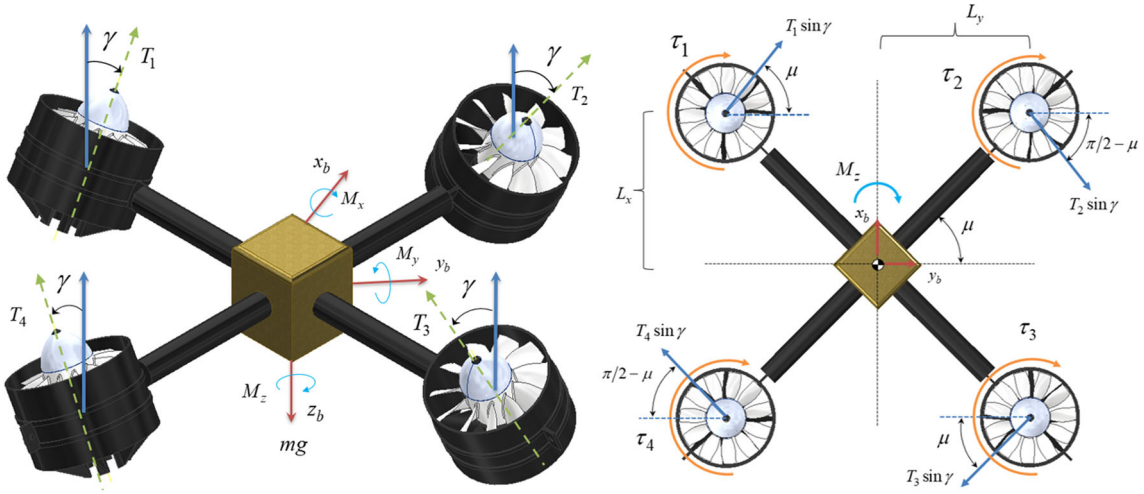

Fig. 2 GMFF's Free Body Diagram, isometric view (left) and top view (right)

where $\mathbf{F_T} \in \Re^3$ and $\mathbf{M}_T \in \Re^3$ represent the external propulsion forces and moments, respectively. $\mathbf{F_g} \in \Re^3$ is the gravitational force acting at the center of mass. $\mathbf{V}_b \in \Re^3$ is the velocity, $m \in \Re$ is the mass of the vehicle, and $\boldsymbol{\omega} \in \Re^3$ is the angular velocity. $J \in \Re^{3\times3}$ is the inertia matrix of the vehicle.

Furthermore, based on Fig. 2, the external propulsion forces can be modeled as:

$$\mathbf{F}_{1T} = \begin{bmatrix} T_1 sin\gamma sin\mu \\ T_1 sin\gamma cos\mu \\ -T_1 cos\gamma \end{bmatrix}, \quad \mathbf{F}_{2T} = \begin{bmatrix} -T_2 sin\gamma sin(\pi/2-\mu) \\ T_2 sin\gamma cos(\pi/2-\mu) \\ -T_2 cos\gamma \end{bmatrix}$$

$$\mathbf{F}_{3T} = \begin{bmatrix} -T_3 sin\gamma sin\mu \\ -T_3 sin\gamma cos\mu \\ -T_3 cos\gamma \end{bmatrix}$$

$$\mathbf{F}_{4T} = \begin{bmatrix} T_4 sin\gamma sin(\pi/2-\mu) \\ -T_4 sin\gamma cos(\pi/2-\mu) \\ -T_4 cos\gamma \end{bmatrix} \tag{3}$$

where $[T_1, T_2, T_3, T_4]$ and $[\tau_1, \tau_2, \tau_3, \tau_4]$ represent the thrust and torque produced by each actuator and μ represents the angle with respect to the y-axis when a thrust tilting angle γ is applied. The total moments are calculated as:

$$\sum \mathbf{M}_T = \mathbf{r}_1 \times \mathbf{F_{1}}_b + \mathbf{r}_2 \times \mathbf{F_{2}}_b + \mathbf{r}_3 \times \mathbf{F_{3}}_b + \mathbf{r}_4 \times \mathbf{F_{4}}_b + \tau_1 + \tau_2 + \tau_3 + \tau_4 \tag{4}$$

with

$$\mathbf{r}_1 = \begin{bmatrix} L_{1x} \\ -L_{1y} \\ L_{1z} \end{bmatrix}, \quad \mathbf{r}_2 = \begin{bmatrix} L_{2x} \\ L_{2y} \\ L_{2z} \end{bmatrix}, \quad \mathbf{r}_3 = \begin{bmatrix} -L_{3x} \\ L_{3y} \\ L_{3z} \end{bmatrix},$$

$$\mathbf{r}_4 = \begin{bmatrix} -L_{4x} \\ -L_{4y} \\ L_{4z} \end{bmatrix} \tag{5}$$

L_x, L_y, and L_z are the distances of each actuator to the center of gravity (CG) and $L = \sqrt{L_x^2 + L_y^2 + L_z^2}$. In this case $L_x = L_{1x} = L_{2x} = L_{3x} = L_{4x}$ and $L_y = L_{1y} = L_{2y} = L_{3y} = L_{4y}$. Additionally, it is valid to assume that the vertical CG distance with respect to the xy plane is small so $L_z = L_{1z} = L_{2z} = L_{3z} = L_{4z} = 0$. The resultant sum of moments at the CG will be:

$$\sum \mathbf{M}_T = \begin{bmatrix} L_y cos\gamma[(T_1 + T_4) - (T_2 + T_3)] \\ L_x cos\gamma[(T_1 + T_2) - (T_3 + T_4)] \\ Lsin\gamma(T_1+T_2+T_3+T_4)+\tau_1+\tau_2+\tau_3+\tau_4 \end{bmatrix} = \begin{bmatrix} M_{xd} \\ M_{yd} \\ M_{zd} \end{bmatrix} \tag{6}$$

and the total sum of forces yields to:

$$\sum \mathbf{F}_T = \begin{bmatrix} sin\gamma(T_1 sin\mu - T_2 cos\mu - T_3 sin\mu + T_4 cos\mu) \\ sin\gamma(T_1 cos\mu + T_2 sin\mu - T_3 cos\mu - T_4 sin\mu) \\ cos\gamma(-T_1 - T_2 - T_3 - T_4) \end{bmatrix} = \begin{bmatrix} F_{xd} \\ F_{yd} \\ F_{zd} \end{bmatrix} \tag{7}$$

The inertia, mass and geometry characteristics of the GMFF are listed in Table 1.

Table 1 Inertial and geometry characteristics of GMFF

Inertial Parameters		Distance from Motor to CG	
J_{xx}(Kg-m^2)	0.012	L_x (m)	0.100
J_{yy}(Kg-m^2)	0.012	L_y (m)	0.100
J_{zz}(Kg-m^2)	0.017	L_z (m)	0.019
m (Kg)	2.04		

3 Control System Architecture

A baseline controller is designed following a feedback linearization technique, also knwon as nonlinear dynamic inversion (NLDI), as a first layer in the proposed control architecture [34–36]. Since exact feedback linearization is not usually achieved, specially in real applications, a second layer includes an adaptive augmentation designed to eliminate residual nonlinearities dynamics that might still be present in the system. This augmentation relies on a model reference architecture that is inspired by the immune response mechanism to internal and external attacks. The advantage of using this bio-inspired approach is the introduction of a distributed self-adaptive system that allows fast response to hostile invasions (e.g. disturbances or failures) [15, 16].

3.1 Baseline Controller

A *Lie*-Derivative based single step inversion approach is used as a baseline controller [36]. Hence, it is convenient to express the kinematics and rotational dynamics in state space form:

$$\dot{\mathbf{x}} = \begin{bmatrix} \dot{\Theta} \\ \dot{\boldsymbol{\omega}} \end{bmatrix} = \begin{bmatrix} \mathbf{g}(\Theta)\boldsymbol{\omega} \\ \mathbf{f}_\omega(\boldsymbol{\omega}) + J^{-1}\mathbf{u}(t) \end{bmatrix} \tag{8}$$

where $\boldsymbol{\omega} = \left[\omega_x, \omega_y, \omega_z\right]^T$ is the angular rates vector, $\Theta = \left[\phi \;\; \theta \;\; \psi\right]^T$ is the attitude angles vector and $\mathbf{u}(t) = \bar{M}_T(t)$ is the vector of control input moments. Defining the functions $\mathbf{g}(\Theta)$ and $\mathbf{f}_\omega(\boldsymbol{\omega})$ based on Euler-kinematics and rotational dynamics we obtain:

$$\mathbf{g}(\Theta) = \begin{bmatrix} 1 & \sin\phi\tan\theta & \cos\phi\tan\theta \\ 0 & \cos\phi & -\sin\phi \\ 0 & \sin\phi\sec\theta & \cos\phi\sec\theta \end{bmatrix} \tag{9}$$

$$\mathbf{f}_\omega(\boldsymbol{\omega}) = -J^{-1}[-\boldsymbol{\omega} \times (J\boldsymbol{\omega})] \tag{10}$$

Equation 8 can be written as an affine nonlinear system:

$$\dot{\mathbf{x}} = \mathbf{F}(\mathbf{x}) + \mathbf{G}(\mathbf{x})\mathbf{u}(t) = \begin{bmatrix} \mathbf{g}(\Theta)\boldsymbol{\omega} \\ \mathbf{f}_\omega(\boldsymbol{\omega}) \end{bmatrix} + \begin{bmatrix} [\mathbf{0}]_{3x3} \\ J^{-1} \end{bmatrix}\mathbf{u}(t) \tag{11}$$

where $\mathbf{x} = [\,\phi \;\; \theta \;\; \psi \;\; \omega_x \;\; \omega_y \;\; \omega_z\,]^T$ and $\mathbf{F}(\mathbf{x}) \in \Re^{6x1}$, $\mathbf{G}(\mathbf{x}) \in \Re^{6x3}$. Assuming full observability of the output vector defined in Eq. 12 and taking the derivative of $\mathbf{y}$ until $\mathbf{u}(t)$ appears explicitly, one can apply direct inversion to obtain an expression of the control laws.

$$\mathbf{y} = h(\mathbf{x}) = \Theta = \left[\phi \;\; \theta \;\; \psi\right]^T \tag{12}$$

Taking the derivative of the output with respect to time, we obtain:

$$\dot{\mathbf{y}} = \frac{d}{dt}h(\mathbf{x}) = \frac{\partial h(\mathbf{x})}{\partial \mathbf{x}}\dot{\mathbf{x}} = \frac{\partial h(\mathbf{x})}{\partial \mathbf{x}}[\mathbf{F}(\mathbf{x}) + \mathbf{G}(\mathbf{x})\mathbf{u}(t)] \tag{13}$$

$$\dot{\mathbf{y}} = \dot{\Theta} = \begin{bmatrix} \dot{\phi} \\ \dot{\theta} \\ \dot{\psi} \end{bmatrix} = \mathbf{g}(\Theta)\,\boldsymbol{\omega}$$

$$= \begin{bmatrix} \omega_x + \omega_y\sin\phi\tan\theta + \omega_z\cos\phi\tan\theta \\ \omega_y\cos\phi - \omega_z\sin\phi \\ \omega_y\sin\phi\sec\theta + \omega_z\cos\phi\sec\theta \end{bmatrix} \tag{14}$$

Taking one more differentiation:

$$\ddot{\mathbf{y}} = \frac{d^2h(\mathbf{x})}{dt^2} = \frac{d\dot{\mathbf{y}}}{dt} = \frac{\partial\dot{\mathbf{y}}}{\partial\mathbf{x}}\dot{\mathbf{x}} = \frac{\partial\dot{\mathbf{y}}}{\partial\mathbf{x}}[\mathbf{F}(\mathbf{x}) + \mathbf{G}(\mathbf{x})\mathbf{u}(t)] \tag{15}$$

$$\ddot{\mathbf{y}} = \begin{bmatrix} \ddot{\phi} \\ \ddot{\theta} \\ \ddot{\psi} \end{bmatrix} = \underbrace{\begin{bmatrix} \dot{\theta}\dot{\phi}\tan\theta + \dot{\theta}\dot{\psi}\sec\theta \\ -\dot{\psi}\dot{\phi}\cos\theta \\ \dot{\theta}\dot{\phi}\sec\theta + \dot{\theta}\dot{\psi}\tan\theta \end{bmatrix}}_{\Lambda(\Theta,\dot{\Theta})} + \underbrace{\begin{bmatrix} 1 & \sin\phi\tan\theta & \cos\phi\tan\theta \\ 0 & \cos\phi & -\sin\phi \\ 0 & \sin\phi\sec\theta & \cos\phi\sec\theta \end{bmatrix}}_{g(\Theta)} \begin{bmatrix} \dot{\omega}_x \\ \dot{\omega}_y \\ \dot{\omega}_z \end{bmatrix} =$$

$$= \Lambda(\Theta, \dot{\Theta}) + g(\Theta)\dot{\omega} \tag{16}$$

Given that Eq. 14 contains the definition of the Euler angle rates as a function of the states (Euler angles and angular rates), this equation can be plugged into Eq. 15 so that the function Λ can be re-written as function of the state vector $\mathbf{x}$:

$$\ddot{\mathbf{y}} = \Lambda(\mathbf{x}) + g(\mathbf{x})\dot{\boldsymbol{\omega}} \tag{17}$$

Moreover, replacing (10) into (17) an expression with explicit input $u(t)$ is obtained:

$$\ddot{\mathbf{y}} = \Lambda(\mathbf{x}) + g(\mathbf{x})\left\{J^{-1}[-\boldsymbol{\omega} \times (J\boldsymbol{\omega}) + \mathbf{u}(t)]\right\} \tag{18}$$

Finally, after inverting the dynamics in Eq. 17, the following control law is obtained:

$$\mathbf{u}(t) = \boldsymbol{\omega} \times (J\boldsymbol{\omega}) + J\left\{g(\mathbf{x})^{-1}[\mathbf{V}(\mathbf{y}, \dot{\mathbf{y}}) - \Lambda(\mathbf{x})]\right\} \tag{19}$$

Applying (19) to the system in Eq. 18 will render the following closed loop linear form:

$$\ddot{\mathbf{y}} = \mathbf{V}(\mathbf{y}, \dot{\mathbf{y}}) = \left[\,u_{v\phi} \;\; u_{v\theta} \;\; u_{v\psi}\,\right]^T \tag{20}$$

where $\mathbf{V}(\mathbf{y}, \dot{\mathbf{y}}) \in \Re^{3x1}$ is a pseudo controller that can be designed to stabilize the closed loop dynamics. The following linear control was chosen as the pseudo controller baseline architecture:

$$\begin{aligned} \ddot{\phi} &= u_{v\phi}(t) = k_\phi k_{D\phi}(\phi_{ref} - \phi) - k_{D\phi}\dot{\phi} \\ \ddot{\theta} &= u_{v\theta}(t) = k_\theta k_{D\theta}(\theta_{ref} - \theta) - k_{D\theta}\dot{\theta} \\ \ddot{\psi} &= u_{v\psi}(t) = k_\psi k_{D\psi}(\psi_{ref} - \psi) - k_{D\psi}\dot{\psi} \end{aligned} \tag{21}$$

The pseudo control gains in Eq. 21 can be calculated using Eq. 22 based on desired dynamic response requirements.

The gains are obtained by comparing the closed loop system with a second order system response.

$$\begin{cases} k_{D\phi} = 2\xi_\phi \omega_{n\phi}, & k_{p\phi} = \omega_{n\phi}/2\xi_\phi \\ k_{D\theta} = 2\xi_\theta \omega_{n\theta}, & k_{p\theta} = \omega_{n\theta}/2\xi_\theta \\ k_{D\psi} = 2\xi_\psi \omega_{n\psi}, & k_{p\psi} = \omega_{n\psi}/2\xi_\psi \end{cases} \tag{22}$$

4 Artificial Immune System based Adaptive Augmentation

Immune system is a complex evolutionary network that compiles several biological mechanisms to protect living organism from hazardous threats. One of the key characteristics is the capability to self-regulate and adapt to new environments through the process of learning from previous encounters. As the immune system gets more robust, it produces the correct amount of specialized cells to countermeasures new or sometimes unknown attacks.

The immune system of living organisms is primarily comprised of two major subsystems, bone marrow and thymus gland. Specialized cells such T-cells and B-cells are produced from these subsystems following a regulatory dynamic process. B-cells are produced in the bone marrow and are the primarily defense against intruders by producing antibodies. T-cells, produced in the thymus gland, are of two types: helper T_h-cells and suppressing T_s-cells. They control and regulate the amount of antibodies present in the bloodstream and guarantee a balance between antibodies and antigens. When an infection is detected, T_h-cells stimulate the generation of antibodies until the threat is reduced. Once the infection is controlled, T_s-cells inhibit the antibody production and therefore a balance is eventually achieved.

Although immune system mechanisms are complex and difficult to characterize, several simpler mathematical models have been proposed [16, 37–39]. Particularly, a model that represents the interaction between B-cells and T-cells can be derived following the difference between the amount of T_h-cells and T_s-cells [39–41]. If the antigens total amount at a given instant time k is defined as $\lambda(k)$, then the response of the T_h-cells can be represented as $T_h(k) = c_1\lambda(k)$ where c_1 is a stimulation constant. Similarly, the production of suppressing T_s-cells can be defined as $T_s(k) = c_2 f(\Delta B(k))\lambda(k)$ where c_2 is a suppression constant, $\Delta B(k))$ is the change of concentration of B-cells, and $f(\Delta B(k))$ is a nonlinear function that relates this change with the amount of T_s-cells. Using these definitions, one can obtain a more general equation that represent these immune interactions:

$$B(k) = K[1 - \eta f(\Delta u(k))]\lambda(k) \tag{23}$$

where K is a reaction rate and $\eta = c_2/c_1$ is a factor that characterizes the dynamic interaction between the T_h-cells and T_s-cells. In general, the stability will depend on the parameter η and the nonlinear function $f(\Delta u(k))$. Notice that Eq. 23 represents a feedback mechanism where the amount of B-cells (input $u(k)$ in the control sense) regulates and minimize the total amount of antigents (error $e(k)$ in the controls sense) present in the the system.

Equation 23 represents a specific case of a more general control structure that models the interaction between T-cells and B-cells as shown in Fig. 3.

where function $P_h(.)$ characterizes the stimulation of antibodies production as a function of error. Function $f_h(.)$ represents the dynamic interaction between helper T_h cells and antigens, and function $f_s(.)$ describes the interaction of the suppressing T_s cells as a function of amount of antibodies present in the system [16].

4.1 Immune Adaptive Augmentation

This paper presents an immune adaptive configuration different from the ones developed in [12, 16, 40]. In our case, a model reference control architecture is used such the immune functions described in [12, 16, 40] are applied to the $\Delta u_x(t)$ (differences in inputs) between the model reference plant and the real plant. The control architecture, named Model Reference based Adaptive Immune System (MRAIS), is also designed to add bounded adaptation such that the absolute stability theorems can be guaranteed for the tracking error dynamics of the closed loop system [42].

Following the analysis in Section 3.1, let's first consider one of the channels in the control design, e.g. roll control. Similarly, this analysis will hold for the other two decoupled attitude channels (pitch and yaw). The goal is that the closed loop dynamics follow the model reference plant with dynamics represented by:

$$\ddot{\phi}_m = u_{x_m}(t) = k_{D\phi}k_\phi(\phi_{ref} - \phi_m) - k_{D\phi}\dot{\phi}_m \tag{24}$$

We can augment the pseudo control law described in Eq. 21 by adding a dynamic adaptation term $u_{AD_x(t)}$ as follows:

$$\begin{aligned} \ddot{\phi} &= u_{v\phi}(t) = u_x(t) + u_{AD_x}(t) \\ \ddot{\phi} &= \underbrace{k_{D\phi}k_\phi(\phi_{ref} - \phi) - k_{D\phi}\dot{\phi}}_{u_x(t)} \\ &\quad + \underbrace{\left\{-k_{e\phi}(t)(\phi - \phi_m) - k_{eD\phi}(t)(\dot{\phi} - \dot{\phi}_m)\right\}}_{u_{AD}(t)} \end{aligned} \tag{25}$$

where the adaptive gains are designed as a function of $f(\Delta u_x(t))$ as:

$$\begin{aligned} k_{e\phi}(t) &= k_{D\phi}k_\phi\eta_x f(\Delta u_x(t)) \\ k_{eD\phi}(t) &= k_{D\phi}\eta_x f(\Delta u_x(t)) \end{aligned} \tag{26}$$

In Eq. 26, η_x is an arbitrary constant and $f(\Delta u_x(t))$ is chosen to be a bounded positive definite nonlinear function

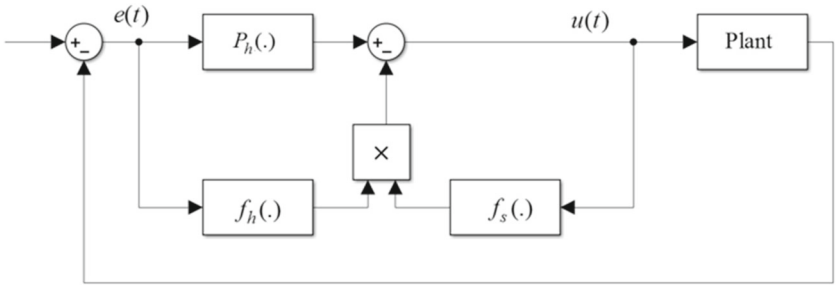

Fig. 3 General architecture for T-B Cells model interaction

that describes the immune response to intruder attacks [12, 40]:

$$f(\Delta u_x(t)) = \left[1 - \frac{2}{e^{\gamma_x[\Delta u_x(t)]^2} + e^{-\gamma_x[\Delta u_x(t)]^2}}\right] \tag{27}$$

where γ_x is a constant. The closed loop plant dynamics will take the form:

$$\begin{aligned}\ddot{\phi} = {} & k_{D\phi}k_\phi(\phi_{ref} - \phi) - k_{D\phi}\dot{\phi} - \eta_x f(\Delta u_x(t)) \\ & \times \left[k_{D\phi}k_\phi(\phi - \phi_m) + k_{D\phi}(\dot{\phi} - \dot{\phi}_m)\right]\end{aligned} \tag{28}$$

The difference in control inputs between the nominal model and the non-adaptive portion of the control law can be defined as:

$$\begin{aligned}\Delta u_x(t) &= u_{m_x}(t) - u_x(t) \\ &= k_{D\phi}k_\phi(\phi_{ref} - \phi_m) - k_{D\phi}\dot{\phi}_m \\ &\quad - \left\{k_{D\phi}k_\phi(\phi_{ref} - \phi) - k_{D\phi}\dot{\phi}\right\} \\ &= k_{D\phi}k_\phi(\phi - \phi_m) + k_{D\phi}(\dot{\phi} - \dot{\phi}_m)\end{aligned} \tag{29}$$

Figure 4 depicts the proposed immunity-based adaptive control architecture.

4.2 Absolute Stability Analysis

If the error is defined as the difference between the actual and the nominal plant:

$$\begin{aligned}e_\phi &= \phi(t) - \phi_m(t) \\ e_{D\phi} &= \dot{\phi}(t) - \dot{\phi}_m(t)\end{aligned} \tag{30}$$

then the difference control input becomes:

$$\Delta u_x(t) = k_{D\phi}k_\phi e_\phi + k_{D\phi}e_{D\phi} \tag{31}$$

Moreover, to find a state space definition of the error dynamics, we can start from the definition of the error provided in Eq. 30:

$$\begin{aligned}\dot{e}_\phi &= \dot{\phi}(t) - \dot{\phi}_m(t) = e_{D\phi} \\ \dot{e}_{D\phi} &= -k_{D\phi}k_\phi e_\phi - k_{D\phi}e_{D\phi} + \eta_x f(\Delta u_x(t)) \\ &\quad \times \left[-k_{D\phi}k_\phi e_\phi - k_{D\phi}e_{D\phi}\right]\end{aligned} \tag{32}$$

Using the definition of Eq. 26 the state space error dynamics reduces to:

$$\begin{bmatrix}\dot{e}_\phi \\ \dot{e}_{D\phi}\end{bmatrix} = \begin{bmatrix}0 & 1 \\ -k_{D\phi}k_\phi & -k_{D\phi}\end{bmatrix}\begin{bmatrix}e_\phi \\ e_{D\phi}\end{bmatrix} + \begin{bmatrix}0 \\ -k_{e\phi}(t)e_\phi - k_{eD\phi}(t)e_{D\phi}\end{bmatrix}$$

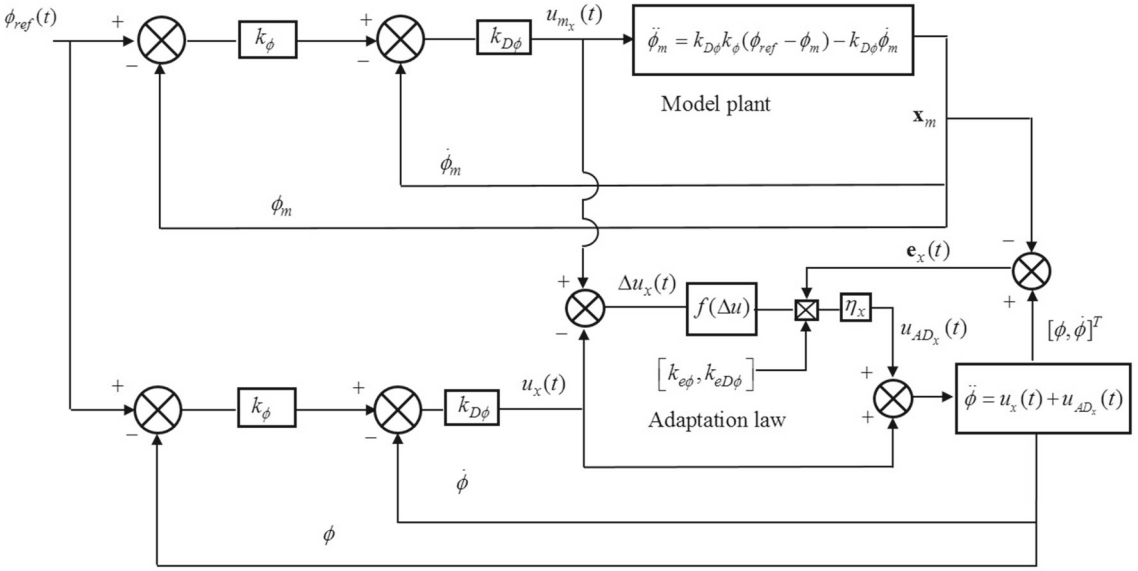

Fig. 4 Model reference AIS adaptive augmentation

The nonlinear error dynamics can be represented as a Lur'e closed loop system as the one shown in Fig. 5 [43] by defining the output of the closed loop system as follows:

$$y_x(t) = [\, k_{D\phi}k_\phi,\ k_{D\phi}\,] \begin{bmatrix} e_\phi \\ e_{D\phi} \end{bmatrix} = \bar{C}_x \mathbf{e}_x = k_{D\phi}k_\phi e_\phi + k_{D\phi}e_{D\phi} = \Delta u_x(t) \tag{33}$$

The nonlinear feedback element $\psi_x(.)$ within the Lur'e system will take the following definition:

$$\begin{aligned} \boldsymbol{\psi}_x(y_x(t)) &= y_x(t)\eta_x f(y_x(t)) \\ &= \eta_x f(\Delta u_x(t)) \left[k_{D\phi}k_\phi e_\phi + k_{D\phi}e_{D\phi}\right] \end{aligned} \tag{34}$$

then, the closed loop error dynamics become:

$$\begin{aligned} \begin{bmatrix} \dot{e}_\phi \\ \dot{e}_{D\phi} \end{bmatrix} &= \begin{bmatrix} 0 & 1 \\ -k_{D\phi}k_\phi & -k_{D\phi} \end{bmatrix} \begin{bmatrix} e_\phi \\ e_{D\phi} \end{bmatrix} \\ &+ \begin{bmatrix} 0 \\ 1 \end{bmatrix} \left[-\boldsymbol{\psi}_x(y_x(t))\right] \\ &\Rightarrow \quad \dot{\mathbf{e}}_x = \bar{A}_x \mathbf{e}_x + \bar{B}_x \left[-\boldsymbol{\psi}_x(y_x(t))\right] \end{aligned} \tag{35}$$

In order to apply the absolute stability theorems the following sector condition must hold globally:

$$\alpha_x y_x(t)^2 \le y_x \boldsymbol{\psi}_x(y_x(t)) \le \beta_x y_x(t)^2, \quad y_x(t) \in [-\infty, \infty] \tag{36}$$

Following this inequality, further analysis can be performed from the nonlinear feedback function ψ_x:

$$\begin{aligned} \boldsymbol{\psi}_x(y_x(t)) &= y_x(t)\eta_x f(y_x(t)) \\ &= y_x(t)\eta_x \left[1 - \frac{2}{e^{\gamma_x [y_x(t)]^2} + e^{-\gamma_x [y_x(t)]^2}}\right] \end{aligned} \tag{37}$$

where $\eta_x, \beta_x, \alpha_x$ are real numbers. In this case, $\alpha_x < \beta_x$ which represents the minimum and maximum linear sectors where the nonlinear function $\boldsymbol{\psi}_x(y_x)$ can lie. Without of loss of generality in this analysis, we can set $\alpha_x = 0$ in Eq. 36:

$$\begin{aligned} 0 &\le y_x(t)\boldsymbol{\psi}_x(y_x(t)) \le \beta y_x(t)^2 \\ 0 &\le \eta_x f(y_x(t)) \le \beta_x \end{aligned} \tag{38}$$

Since $\sup\{f(y_x(t))\} = 1$, the following inequality holds:

$$\begin{aligned} 0 &\le \eta_x f(y_x(t)) \le \eta_x \sup[f(y_x(t))] \le \beta_x \\ 0 &\le \eta_x f(y_x(t)) \le \eta_x \le \beta_x \end{aligned} \tag{39}$$

Therefore, given that $\beta_x <= \infty$ as long as η_x is a real positive scalar, the sector condition will hold globally. Figure 6 shows that the non-linearity behaviour for the case $\eta_x = 1$, it can be seen the sector condition holds.

Furthermore, the Circle Criterion can be applied as an extension of Popov's theorem. As described by Khalil in [43], this theorem establishes that a system with a feedback sector nonlinearity that holds globally will be absolutely stable if :

$$\mathrm{Re}[1 + \beta_x G_x(j\omega)] > 0, \quad \rightarrow \quad \mathrm{Re}[G_x(j\omega)] > -\frac{1}{\beta_x} \forall \omega \in R \tag{40}$$

Equation 40 implies that the Nyquist plot of $G_x(j\omega)$ must lie to the right hand side of the vertical line defined by $\mathrm{Re}(s) = -1/\beta_x$. The following more conservative condition will also met the Circle Criterion:

$$\mathrm{Re}[G_x(j\omega)] > 0, \quad \forall \omega \in R \tag{41}$$

Consequently, the transfer function $G_x(j\omega)$ must be specified in frequency domain as follows:

$$\begin{aligned} G_x(j\omega) = C(sI - \bar{A}_x)^{-1}\bar{B}_x &= \frac{k_{D\phi}(j\omega) + k_{D\phi}k_\phi}{(j\omega)^2 + k_{D\phi}(j\omega) + k_{D\phi}k_\phi} = \\ &= \frac{k_{D\phi}(j\omega) + k_{D\phi}k_\phi}{-\omega^2 + k_{D\phi}(j\omega) + k_{D\phi}k_\phi} \end{aligned} \tag{42}$$

where the real part of the transfer function results in:

$$\mathrm{Re}\{G_x(j\omega)\} = \frac{k_\phi^2 k_{D\phi}^2 + \omega^2\left(k_{D\phi}^2 - k_\phi k_{D\phi}\right)}{k_\phi^2 k_{D\phi}^2 + \omega^2\left(k_{D\phi}^2 - 2k_\phi k_{D\phi}\right) + \omega^4} \tag{43}$$

Therefore, to obtain a positive real part of the transfer function, the following inequalities must hold:

$$k_{D\phi} > 2k_\phi \tag{44}$$

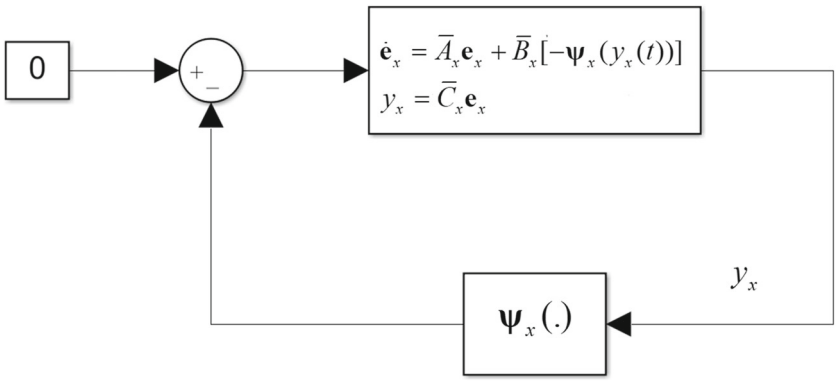

Fig. 5 Closed loop roll error dynamics seen as a Lur'e type system

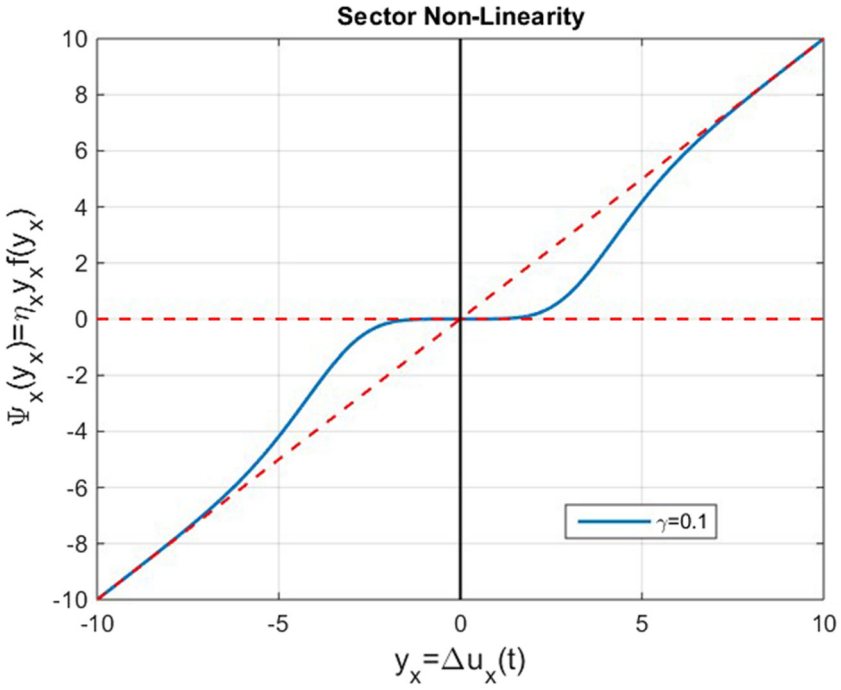

Fig. 6 Sector nonlinearity

$$k_{D\phi} > k_{\phi} \tag{45}$$

The condition in Eq. 44 is more conservative and also meets the condition in Eq. 45 so it is the one selected.

In order to prove absolute stability the transfer function $G_x(s)$ also needs to be Hurwitz. To verify this condition, the following analysis in s-domain is performed:

$$G_x(s) = \bar{C}_x(sI - \bar{A}_x)^{-1}\bar{B}_x = \frac{k_{D\phi}s + k_{D\phi}k_{\phi}}{s^2 + k_{D\phi}s + k_{D\phi}k_{\phi}} \tag{46}$$

The gains in the transfer function denominator must be positive, which implies that the following conditions must be met:

$$\begin{cases} k_{D\phi} > 0 \\ k_{\phi}k_{D\phi} > 0 \end{cases} \tag{47}$$

Consequently, it can be concluded that if the conditions in Eqs. 44 and 47 are met then the closed loop error dynamics of the adaptive system in Fig. 4 will be absolutely stable.

5 Performance Metrics and Numerical Simulations

To assess the effectiveness of the proposed control architecture, a set of metrics were used that include actuation performance and tracking error for attitude, angular rates, velocity and position. As an example, Eq. 48 represents the attitude performance metric as the measurement of accumulated tracking error in the attitude angle.

$$\tilde{e}_{\Theta} = \frac{1}{C\Theta}\left(\sum_{i=1}^{3}\sqrt{\int_0^T e_i(t)dt}\right) \tag{48}$$

Similar equations can be used for angular rates $\tilde{e}_{\Delta\Omega}$, velocity $\tilde{e}_V$ and position $\tilde{e}_P$ performance metrics.

The actuation performance index metric measures the activity of the thrust actuation and thrust vectoring required to perform the commanded maneuvers and maintain stability of the vehicle. It can be defined as:

$$\tilde{s} = \frac{1}{C\Delta S}\left(\sum_{i=1}^{4}\sqrt{\int_0^T S_i(t)dt}\right) \tag{49}$$

where e_i is the tracking error of the i^{th} attitude, velocity, position and angular rate states. S is the actuation that combines power and thrust vectoring at each thruster. A set of normalization factors $C\Theta$, $C\Delta\Omega$, CV, CP and $C\Delta$S are also defined based on the worst performance case. The

Table 2 Control gains of the baseline controller

$K_{D\phi} = 16$	$K_{\phi} = 6.58$	$K_{V_x} = 0.4$	$K_{P_x} = 0.16$
$K_{D\theta} = 16$	$K_{\theta} = 6.58$	$K_{V_y} = 0.4$	$K_{P_y} = 0.16$
$K_{D\psi} = 16$	$K_{\psi} = 6.58$	$K_{V_z} = 0.4$	$K_{P_z} = 0.16$

Table 3 Adaptive augmentation parameters

ξ_x	0.78	η_x	5.5	$T_{sx}(s)$	0.5
ξ_y	0.78	η_y	5.5	$T_{sy}(s)$	0.5
ξ_z	0.78	η_z	3.0	$T_{sz}(s)$	0.5

individual metrics can then be combined to obtain a Global Performance Index P_I:

$$P_I = 1 - (w_1\tilde{e}_\Theta + w_2\tilde{e}_{\Delta\Omega} + w_3\tilde{e}_V + w_4\tilde{e}_P + w_5 S) \quad (50)$$

where w_1, w_2 , w_3 , w_4 and w_5 are weights chosen by the user to determine the contribution of each performance metric. A P_I of 1.0 corresponds to the best performance.

Numerical simulations were performed to evaluate the control architecture under nominal and failure conditions. The mission was designed such that the vehicle is commanded to track a set of pre-set waypoints. A failure was then introduced at 45 seconds after the vehicle takes off, and it was modeled as a saturation at 4.6% of maximum power in one of the thrusters with a tilting angle locked at 10 degrees in the same thruster. Tables 2 and 3 outline the control parameters for the baseline and adaptive augmentation control laws.

Figure 7 shows examples of the commanded trajectory and tracking performance for both, baseline and adaptive controllers under nominal conditions. Under nominal condition both controllers are able to track the commanded trajectory with an acceptable and similar performance.

Figure 8 shows the tracking performance of the controllers while the vehicle operates under failure condition. In this scenario, the tracking is significantly improved when MRAIS augments the baseline controller compared to the baseline controller alone, e.g., the baseline controller performances poorly to the point that the vehicle is not able to complete the mission and the simulation stops when the it reaches the 7th waypoint. As an additional example and to better visualize the effect of the adaptation, Fig. 9 shows the performance of both controllers for angular rates. After the failure is injected, MRAIS controller is capable to maintaining tracking of the commanded rates with minimum error whereas the NLDI controller induces a significant amount of tracking error. Additionally, Fig. 10 shows an example of time history of the adaptive gains for pitch and yaw controls. Once the failure takes effect at 45 seconds, the adaptation gains show activation to compensate the failure. Table 4 summarizes the performance metrics for both cases, nominal and failure. It is notable that the adaptive augmentation provides a better performance with an accumulative normalized PI of 86%, compared to that of the baseline control law with 0.6% PI.

6 Hardware Implementation

Two approaches were considered for real-time hardware implementation, the first one consists on a Hardware in the Loop (HIL) setup which includes a host computer that runs the mathematical model of the vehicle dynamics and a target computer that runs the designed control laws at 100Hz. The main goal of the HIL setup was to evaluate the dynamic performance of the novel adaptive control algorithm on the same type of space exploration missions presented in section 5 while running the control laws on the target hardware.

The second setup involved the development of a research vehicle prototype developed by NASA named "Gimbaled Mini-Free Flyer" (GMFF). This test-bed incorporates a real flight control computer (Pixhawk 1), real sensors and actuators in the loop. The main goal of this setup was to assess the attitude tracking capabilities of the proposed adaptive control laws in a gimbaled setup that allows motion of the vehicle on its three axis of rotation (roll, pitch and yaw).

6.1 Hardware in the Loop Implementation Results

• Condition 1 - nominal: this test was designed to assess the control performance given a change of inertia while the vehicle is commanded to track a trajectory defined by nine waypoints. At waypoint 5, the vehicle is commanded to land and take a mass sample of 200g. The exta mass is placed at $\overrightarrow{r} = [0\ 0.152\ 0.152]m$ from the vehicle's CG. This

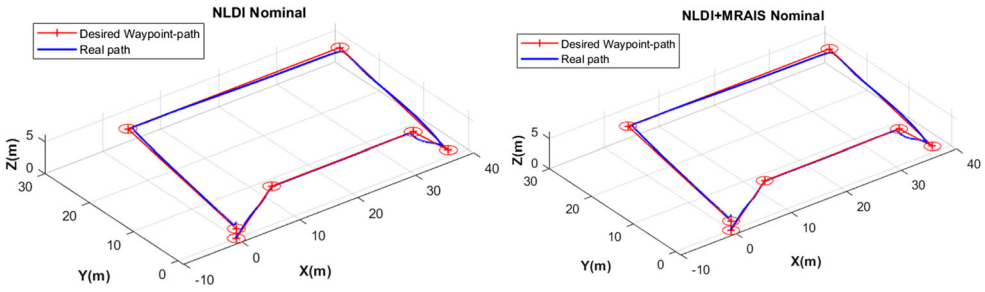

Fig. 7 Position tracking under nominal condition (Left: NLDI, Right: NLDI+MRAIS)

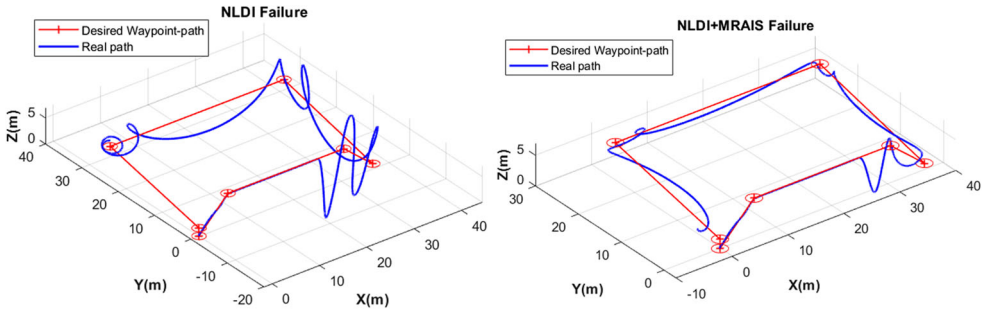

Fig. 8 Position tracking under failure condition (Left: NLDI, Right: NLDI+MRAIS)

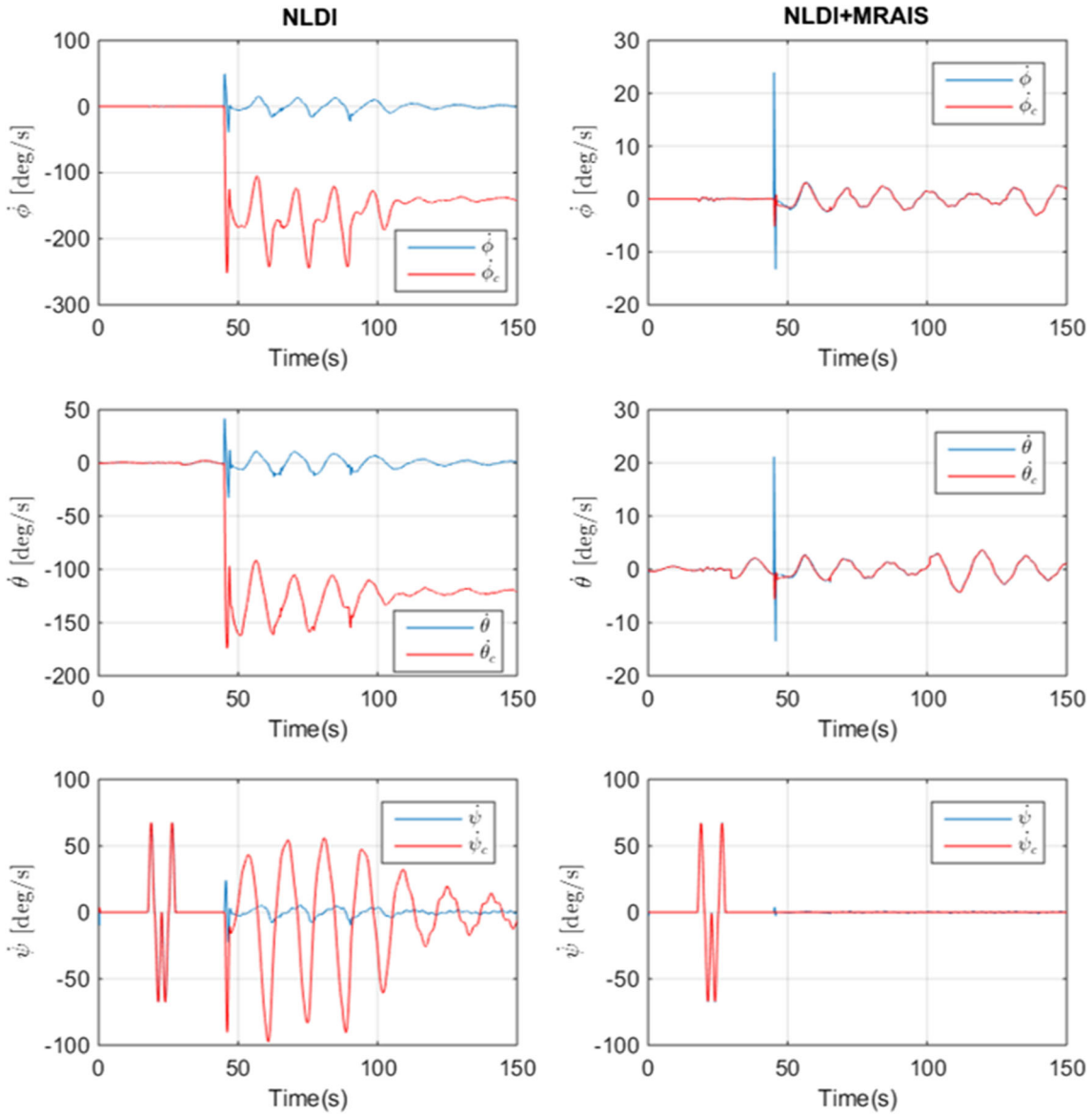

Fig. 9 Pitch rate tracking under failure condition (Left: NLDI, Right: NLDI+MRAIS)

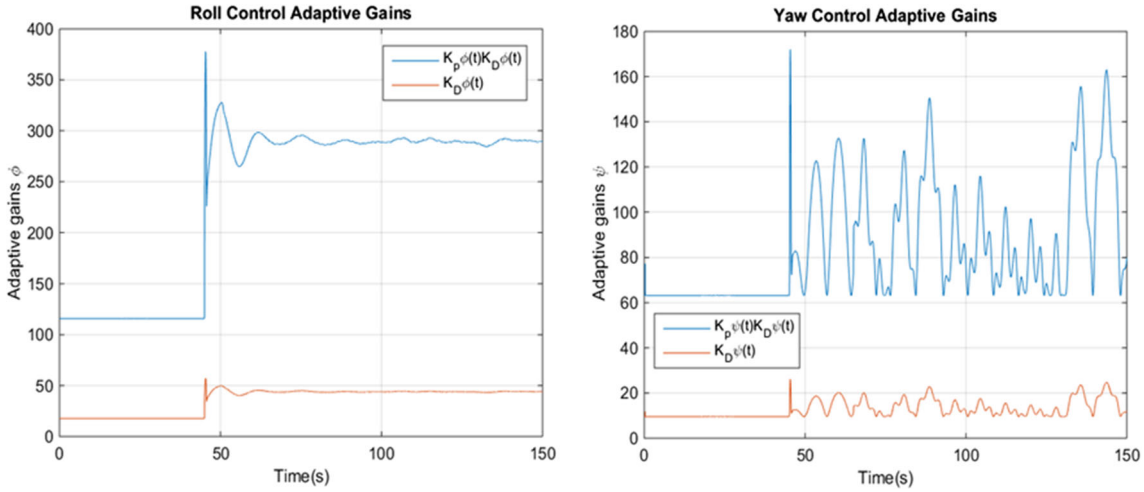

Fig. 10 MRAIS adaptive gains (left: roll control, right: yaw control)

extra mass produces the following change of inertia and CG location:

$$\Delta J_2 = \begin{bmatrix} 0.0092 & 0 & 0 \\ 0 & 0.0046 & 0 \\ 0 & 0 & 0.0046 \end{bmatrix} Kg.m^2;\ \Delta \overrightarrow{r}_2 = \begin{bmatrix} 0 & 0.0017 & 0.0017 \end{bmatrix} m \quad (51)$$

• Condition 2 - sampling extra weight: this mission follows the same profile of Mission 1, but the vehicle is now loaded with an extra mass of 800g at the location $\overrightarrow{r} = [0\ 0.152\ 0.152]m$ from the vehicle's CG that consequently changes the inertia and CG location as:

$$\Delta J_2 = \begin{bmatrix} 0.0355 & 0 & 0 \\ 0 & 0.0177 & 0 \\ 0 & 0 & 0.0177 \end{bmatrix} Kg.m^2;\ \Delta \overrightarrow{r}_2 = \begin{bmatrix} 0 & 0.0067 & 0.0067 \end{bmatrix} m \quad (52)$$

• Condition 3 - thruster reduced efficiency: similar to nominal case in Mission 1, the vehicle is commanded to follow the same trajectory while is loaded with an extra mass of 200g at $\overrightarrow{r} = [0\ 0.152\ 0.152]m$ from the CG. However, while performing the commanded maneuvers, power on thruster 1 slowly starts reducing efficiency by decreasing its power to 40% from the maximum force within a period of 150 seconds.

Table 5 summarizes the accumulated global performance index obtained from the three missions. Results from a typical PID controller have also been included for comparison purposes. The results show that MRAIS outperforms the other two controllers achieving more than 50% increase in performance for all three missions.

Table 4 Performance metrics for numerical simulations

Performance Index	Nominal		Failure	
	NLDI	MRAIS	NLDI	MRAIS
Angular Rates	1.05	0.24	268.98	2.25
Attitude	1.90	0.03	41.28	9.61
Velocities	1.05	1.05	11.76	3.68
Position	31.61	3.61	42.84	33.67
PI	0.63	0.67	0.004	0.56
Normalized PI	0.95	1.00	0.006	0.86

6.2 Experimental Results on Gimbaled Mini Free Flyer

As mentioned before, the GMFF is a vehicle prototype mounted on a gimbal that allows the vehicle rotate on its three axis (see Fig. 1), in order to demonstrate attitude tracking capabilities. The system is equipped with four Electric Ducted Fans (EDF) capable of producing 4.8kg of total thrust and four servos that allow rotational motion of each of the EDFs.

Results were obtained from tests where the EDF#3 is fully jammed at 67 seconds while the vehicle is commanded to track smooth roll and yaw reference inputs.

Figure 11 presents a qualitative comparison of the numerical simulation and the experimental results on the

Table 5 Performance metrics for HIL simulations

Control Laws	Test Condition		
	Nominal	Extra Mass	Failure in T1
PID	0.490	0.425	0.006
NLDI	0.611	0.531	0.121
MRAIS	1.000	0.953	0.813

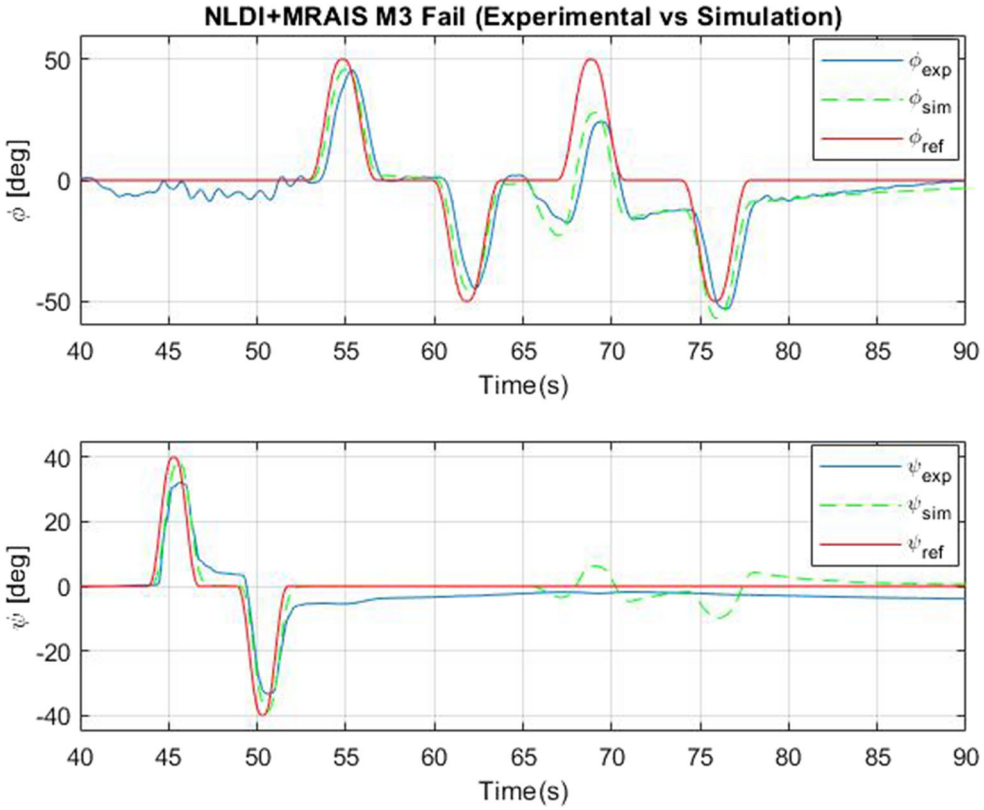

Fig. 11 Experimental vs simulation results, failure in EDF 3

GMFF vehicle. It can be seen that the numerical simulation closely matches the real implementation results. The differences in the responses can be attributed to unmodeled dynamics such as friction of some of the mechanical components present in the experimental setup (i.e. gimbals and bearings).

Figure 12 presents the time history of angular rate for both, the baseline and the adaptive augmentation. Significant improvement is achieved by the adaptive augmentation with less oscillatory dynamics and higher tracking performance. The results in Fig. 13 also shows similar behaviour for roll angle tracking. It is clear that the adaptive augmentation outperforms the NLDI with improved tracking under abnormal conditions.

Figure 14 shows activity of the roll angle adaptive gains. As predicted from the numerical simulation results, it is notable the activation of the adaptive gains once the failure takes effect on the system dynamics.

Further tests were performed with a mass of 130 grams added in one of the arms of the vehicle after 5 seconds from the first commanded maneuver, while the controller is tracking a smooth cycloid roll command. As shown in Figs. 15 and 16, the angular rate and roll angle tracking performance are improved by the adaptive augmentation. However, it is also noticeable how this type of disturbance, that corresponds to a significant changes in vehicle's inertia, represents a more challenge case, even for the adaptive augmentation.

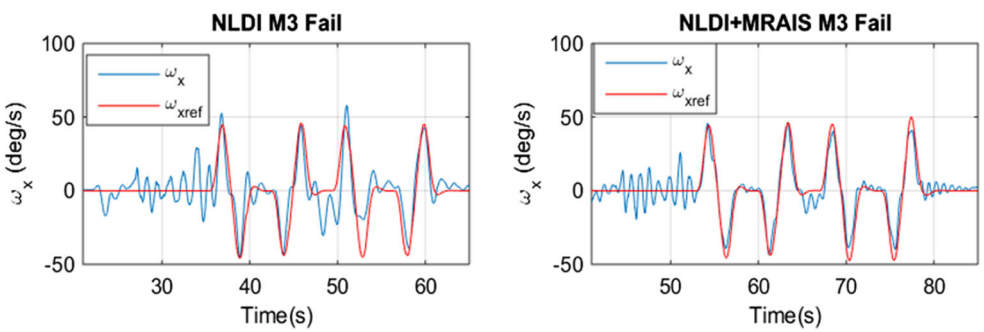

Fig. 12 Angular rates tracking under failure in EDF 3

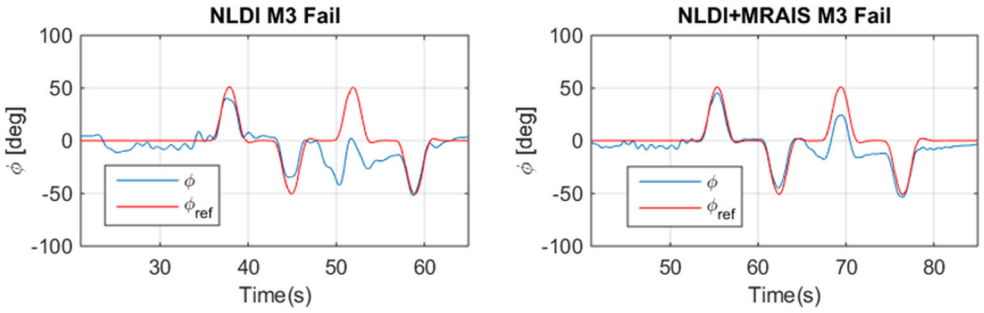

Fig. 13 Roll angle tracking under failure in EDF 3

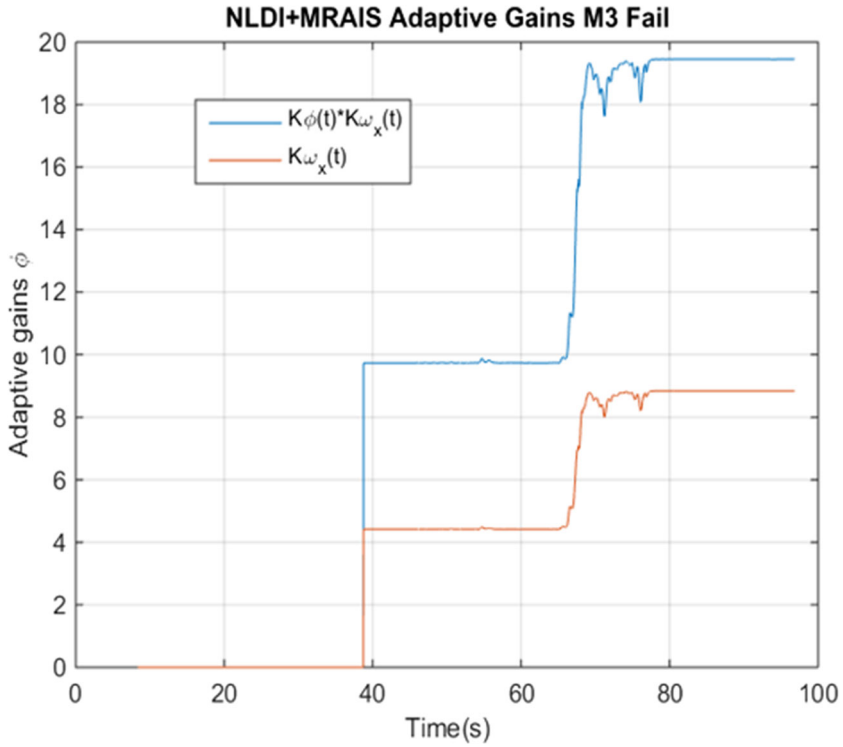

Fig. 14 Adaptive gains activation under failure in EDF 3

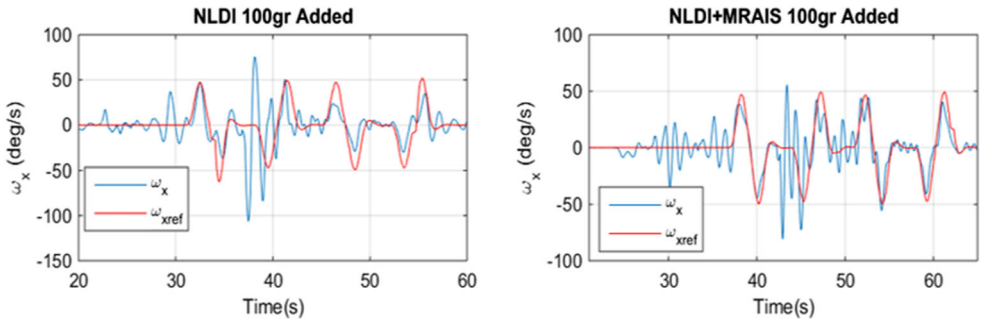

Fig. 15 Angular rates tracking performance for case of adding 130g on left arm

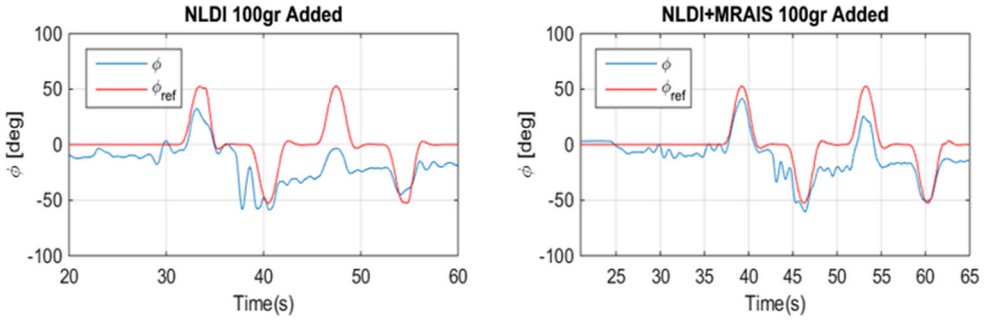

Fig. 16 Roll angle tracking performance for case of adding 130g on left arm

7 Conclusions

A novel control adaptation based on immunity based mechanisms has been introduced in this paper. The MRAIS control architecture combines a feedback linearization approach as a baseline controller with an adaptive scheme augmentation inspired by immune mechanisms of living organisms. A theoretical framework and proof of absolute stability using Circle Criterion were presented in this paper.

Numerical simulations were performed using different flight scenarios and the performance of the proposed control laws evaluated and analyzed. Results show that the proposed control augmentation provide a promising alternative tool that significantly enhance the baseline control with adaptability characteristics.

Validation of these results were further obtained using a HIL setup and actual implementation using a vehicle research test-bed. In all scenarios, the adaptive augmentation is capable of rejecting failures and compensating system uncertainties or unmodeled dynamics. It is noteworthy, however, that implementation shows more conservative performance compared to that of simulation. This might be explained by the fact that some basic assumptions were made in the analytical proofs that were not explicitly considered in the real case implementation. For example, continuous time domain was assumed in the analytical design of the controller which might cause discrepancies in the dynamic response if the real system is not properly sampled at a high frequency. Additionally, the delay between the commanded input and the actuation response, typical in control applications, was not included in the analytical development, although it was included in the numerical simulations. Possible future work would include stability proof analysis considering the effect of the actuator time response, which indeed will allow to obtain more realistic gain bounds to maintain stable operation of the system.

Acknowledgements The authors would like to thank the support and funding provided by NASA to perform the research study under contract number NNX14CK09P.

Author Contributions All authors of this research paper, Dr. Andres Perez and Dr. Hever Moncayo, have directly and equally participated in the planning, execution, or analysis of this study.

Funding This research work was funded by National Aeronautics and Space Administration under contract number NNX14CK09P

Data Availability Some or all data, models, or material used during the study may only be provided with restrictions upon request.

Code Availability Some or all codes generated during the study may only be provided with restrictions upon request.

Declarations

Ethics approval Not applicable as this study does not contain biological applications.

Consent to participate All authors of this research paper have consented to participate in the research study.

Consent for Publication All authors of this research paper have read and approved the final version submitted.

Conflict of Interests The authors declare that they have no conflict of interest.

References

1. Garcia, D., Perez, A., Moncayo, H., Rivera, K., Betancur, Y., DuPuis, M., Mueller, R.: Spacecraft heath monitoring using a biomimetic fault diagnosis scheme. J. Aerosp. Inf. Syst. **15**(7), 396–413 (2018)
2. Perez, A., Moncayo, H., Prazenica, R., Zacny, K., Mueller, R., Dupuis, M., Ebert, T.: Control laws development for a free-flying unmanned robotic system to support interplanetary bodies prospecting and characterization missions. In: AIAA SciTech Conference, San Diego, CA (2016)
3. Zacny, K., Yaggi, B., Spring, J., Chu, P., Mueller, R., Ebert, T., Dupuis, M., Moncayo, H., Prazenica, R.: Sample acqusition systems for a free-flying unmanned robotic system to support interplanetary bodies prospecting and characterization missions. In: AIAA SciTech Conference, San Diego, CA (2016)
4. Prazenica, R., Kern, K., John, T., Moncayo, H., Zacny, K., Mueller, R., Ebert, T., Dupuis, M.: Vision-aided navigation for a free-flying unmanned robotic system to support interplanetary bodies prospecting and characterization missions control. In: AIAA SciTech Conference, San Diego, CA (2016)
5. Deshpande, A.ditya.M., Kumar, R.umit., Minai, A.A., Kumar, M.anish.: Developmental reinforcement learning of control policy of a quadcopter UAV with thrust vectoring rotors. In: ASME Dynamic Systems and Control Conference DSCC, Pittsburgh, Pennsylvania (2020)

6. Betancur, Y., Moncayo, H.: Spacecraft testbed to support control system design for space missions. In: AIAA SciTech Conference, GNC (2021)
7. Edwards, C., Lombaerts, T., Smaili, H.: Fault Tolerant Flight Control: A Benchmark Challenge. Springer, Berlin (2010)
8. Khalastchi, E., Kalech, M.: On fault detection and diagnosis in robotic systems. ACM Comput. Surv. **51**(1), 9 (2018)
9. Ibrahim, S., Ayman, M., Zeidan, A.: Machine learning techniques for satellite fault diagnosis. Ain Shams Eng. J. (2019)
10. Dias, P., Zhou, Y., Van Kampen, E.: Intelligent Nonlinear adaptive flight control using incremental approximate dynamic programming. In: AIAA, Session: Advances in Adaptive Control Systems IV (Invited), Published Online, pp. 2019–2339 (2019)
11. Ibrahim, S., Ahmed, A., Eldin, M., Ziedan, I.: Machine learning techniques for satellite fault diagnosis. Ain Shams Eng. J. (2019)
12. Mo, H., Fu, D., Xu, L.: Research of a kind of improved immune controller based immune network. Int. J. Intell. Comput. Cybern. **3**(2), 310–333 (2014)
13. Zhao, G., Shen, Y., Zhang, L.: Research on CNC machine tool fuzzy immune PID position controller. Res. J. Appl. Sci. Eng. Technol, Maxwell Scientific Organization **212**, 209 (2013)
14. Coulter, N., Moncayo, H.: Comparison of optimal and bio-inspired adaptive control laws for spacecraft sloshing dynamics. J. Spacecr. Rockets **57**(1) (2020)
15. Benjamini, E.: Immunology A Short Course. Wiley-List Publications, New York (1992)
16. Mo, H.: Handbook of Research on Artificial immune systems and natural computing. Med. Inf. Sci., 262–303 (2008)
17. Mehare, V., Thakur, R.S.: Data mining models for anomaly detection using artificial immune system. In: Proceedings of International Conference on Recent Advancement on Computer and Communication. Lecture Notes in Networks and Systems, vol. 34. Springer, Singapore (2018). https://doi.org/10.1007/978-981-10-8198-9-44
18. Timmis, J., Andrews, P., Hart, E.: On artificial immune systems and swarm intelligence. Swarm. Intell. **4**, 247–273 (2010). https://doi.org/10.1007/s11721-010-0045-5
19. Daudi, J.: An overview of application of artificial immune system in swarm robotic systems. Autom. Control. Intell. Syst. **3**(2), 11–18 (2015). https://doi.org/10.11648/j.acis.20150302.11
20. Zhao, F., Li, G., Yang C., Abraham, A., Liu, H.: A human–computer cooperative particle swarm optimization based immune algorithm for layout design. Neurocomputing **132**, 68–78 (2014). ScienceDirect
21. Xia, M., Song, Y.: Immune network-based swarm intelligence and its application to unmanned aerial vehicle swarm coordination. Neurocomputing **125**, 134–141 (2014). ScienceDirect
22. Coello, C.A.C., Cortés, N.C.: Solving multiobjective optimization problems using an artificial immune system. Genet. Program Evolv. Mach. **6**, 163–190 (2005). https://doi.org/10.1007/s10710-005-6164-x
23. Zhang, W., Yen, G.G., He, Z.: Constrained Optimization via Artificial Immune System. IEEE Trans Cybern. **44**(2), 185–98 (2014). https://doi.org/10.1109/TCYB.2013.2250956
24. Parra dos Anjos Lima, F., Chavarette, F.R., dos Santo e Souza, A., Silva Frutuoso de Souza, S., Martins Lopes, M.L.: Artificial immune systems with negative selection applied to health monitoring of aeronautical structures. Adv. Mater. Res. **871**, 283–289 (2014)
25. Anaya, M., Tibaduiza, D., Pozo, F.: Data driven methodology based on artificial immune systems for damage detection
26. Lau, H.Y.K., Qiu, X.: An artificial immune systems (AIS)-based unified framework for general job shop scheduling. IFAC Proc. Vol. **47**(3), 6186–6191 (2014)
27. Wang, M., Feng, S., He, C., Li, Z., Yu, X.: An artificial immune system algorithm with social learning and its application in industrial pid controller design. https://doi.org/10.1155/2017/3959474 (2017)
28. Deng, L., Ma, X., Gu, J., Li, Y.: Mobile robot path planning using polyclonal-based artificial immune network. J. Control Sci. Eng., Hindawi Publishing Corporation **2013**, 13 (2013). https://doi.org/10.1155/2013/416715
29. Yuan, M., Jiang, Y., Hua, X.: A real-time immune planning algorithm incorporating a specific immune mechanism for multi-robots in complex environments. In: Proceedings of the Institution of Mechanical Engineers, Part I: Journal of Systems and Control Engineering (2017). https://doi.org/10.1177/0959651816677198
30. Suliman, S.I., Abd Shukor, M.S., Kassim, M., Mohamad, R., Shahbudin, S.: Network intrusion detection system using artificial immune system (AIS). In: 3rd International Conference on Computer and Communication Systems (ICCCS). Nagoya, Japan, pp. 178–182 (2018). https://doi.org/10.1109/CCOMS.2018.8463274
31. Farouq, O., Maryam, L., Dawood, H.: Model reference adaptive control based on a self-recurrent wavelet neural network utilizing micro artificial immune systems. Al-Khawarizmi Eng. J. **13**(2), 107–122 (2017)
32. Siceloff, S.: Extreme Access flyer to take planetary exploration airborne, nasa.gov. [Online]. Available: https://www.nasa.gov/feature/extreme-access-flyer-to-take-planetary-exploration-airborne. [Accessed 24 October 2020] (2015)
33. Verberne, J., Betancur, A., Rivera, K., Coulter, N., Moncayo, H.: Comparison of MRAC and L1 adaptive controllers for a gimbaled mini-free flyer. In: AIAA SciTech Conference. San Diego, California (2019)
34. Tipan, S., Theodoulis, S., Thai, S., Proff, M.: Nonlinear dynamic inversion flight control design for guided projectiles. J. Guid. Control Dyn. **43**(5) (2020)
35. Smeur, E., de Croon, G.E., Chu, Q.: Cascaded incremental nonlinear dynamic inversion for MAV disturbance rejection. Control. Eng. Pract. **73**, 79–90 (2018)
36. Yuan, R., Guoliang, F., Yi, J., Yu, W.: Robust attitude controller for unmanned aerial vehicle using dynamic inversion and extended state observer. In: Second International Conference on Intelligent Computation Technology and Automation. Beijing, China, pp. 850–853 (2009)
37. Jian-Min, S., Peng-Tao, Z.: Immune feedback strategy in an electronic throttle control system. J. Highway Transp. Res. Dev. **13**(3) (2019)
38. Wang, W., Gao, X.Z., Wang, C.A.: A new immune PID controller based on immune tuning, advanced intelligent computing theories and applications. ICIC 2007. In: Communications in Computer and Information Science, vol. 2 (2017)
39. Perez, A., Moncayo, H., Perhinschi, M.G., Al Azzawi, D., Togayev, A.: A bio-inspired adaptive control compensation system for an aircraft outside bounds of nominal design. J Dyn Syst Meas Control, ASME **137** (2015)
40. Takahashi, K., Yamada, T.: Application of an immune feedback mechanism to control systems. JSME Int. J. **41**(Series C), 184–191 (1998)
41. Liu, X., Chen, X., Zheng, X., Li, S., Wang, Z.: Development of a GA-fuzzy-immune PID controller with incomplete derivation for robot dexterous hand. Sci. World J. https://doi.org/10.1155/2014/564137 (2014)
42. Perez, A.: Development of fault tolerant adaptive control laws for aerospace systems. Ph.D. Dissertation, Aerospace Engineering Department Embry-Riddle Aeronautical University (2016)
43. Khalil, H.K.: Nonlinear Systems. Prentice Hall, New Jersey (1996)

Andres Perez received his B.S and MS in Mechanical Engineering from Universidad de los Andes (Bogota, Colombia) and his doctorate in Aerospace Engineering from Embry-Riddle Aeronautical University (Daytona Beach, Florida). During his doctorate he focused on the development of novel bio-inspired fault tolerant adaptive controls while participating in various projects sponsored by the department of defense DARPA and NASA. Dr. Perez is currently a systems engineer, control law analyst and product owner at Collins Aerospace flight controls department. In his current role he actively participates in the development and testing of the Autopilot, Flight Guidance and Autothrottle software applications for different commercial and military aviation aircraft like the Airbus A220, Viking Water bomber, Global 7500, French E-3F AWACS, Embraer KC-390 and Xian MA700. He has also recently participated in multiple innovation projects for the development of vision based Autoland and resilient autopilot systems.

Hever Moncayo is an Associate Professor with the Aerospace Engineering Department at Embry-Riddle Aeronautical University. He earned a Bachelor of Science in Engineering Physics, a Master of Science in Mechanical Engineering and a Ph.D. in Aerospace Engineering. As a researcher, Dr. Moncayo has focused his efforts to advanced research and development of algorithms for guidance, navigation and control, including simulation of comprehensive/integrated methodologies for intelligent/adaptive fault tolerant flight control systems. He has contributed to the study of technologies to ensure increased aerospace system safety operation and autonomy by providing alternative and innovative comprehensive solutions. Dr. Moncayo is director of the Advanced Dynamics and Control Laboratory, a senior member of American Institute of Aeronautics and Astronautics (AIAA), member of the AIAA Intelligent Systems Committee, and an Associate Editor of the Journal Aerospace Science and Technology.